Available online at www.sciencedirect.com
ScienceDirect
Journal of Power Sources 159 (2006) 1494–1509
JOURNAL OF POWER SOURCES
www.elsevier.com/locate/jpowsour

Energy scavenging for small-scale unmanned systems

James P. Thomas [a,*], Muhammad A. Qidwai [b], James C. Kellogg [c]

[a] *Multifunctional Materials Branch, Code 6350, Naval Research Laboratory, 4555 Overlook Avenue, SW, Washington, DC 20375, USA*
[b] *NRL Washington Operations, SAIC, 1220 12th Street, SE, Suite 140, Washington, DC 20003, USA*
[c] *Off-board Countermeasures Branch, Code 5710, Naval Research Laboratory, 4555 Overlook Avenue, SW, Washington, DC 20375, USA*

Received 7 December 2005; accepted 17 December 2005
Available online 24 February 2006

Abstract

Several energy scavenging concepts are reviewed and analyzed to determine their potential for supplementing the on-board energy of small electric unmanned systems to enable increases in endurance and range. Photonic (solar), kinetic-flow (wind), thermal, and electromagnetic sources of energy are considered as well as autophagous structure–power concepts that allow for energy generation through self-consumption of system structure. Notional designs for each scavenging concept are evaluated with regard to their power collection capability and multifunctional potential. Power collection levels ranging from fractions of a watt to tens of watts are possible depending on the weight and size allowed for the energy collection or autophagous storage elements and the efficiency of conversion from scavenged energy to system electrical energy. An analysis methodology is developed to link energy scavenger performance to changes in unmanned system performance. The methodology is demonstrated by analyzing solar scavenging on unmanned air vehicles as a means of extending the flight endurance time.

Keywords: Autophagous; Induction-antenna; Multifunctional; Photovoltaic; Thermoelectric; Wind-generator

1. Introduction

A wide variety of large and small unmanned systems are being developed and used by government and industry for sensing (e.g., reconnaissance, surveillance, chemical/biological/nuclear) and other types of missions on land, in the air, in or on the water, and in space. Small unmanned systems, defined here as those that can easily be carried by one person, are often electrically powered using primary or secondary battery cells. They may be mobile or immobile, and if mobile, their range can vary from meters to tens of kilometers. Critical system metrics such as endurance and range are directly related to the system's power requirements and the amount of energy carried on-board. The system's size, weight, and operational requirements related to mobility, range, and time-on-station dictate the power needed, and the on-board energy storage capacity is governed by the volume and weight available for the energy storage device(s).

Supplementing the on-board energy stores with energy scavenged[1] in-the-field can provide a new capability for extending the endurance and range of electric-powered unmanned systems. We examine the feasibility of scavenging energy from a variety of natural and artificial energy sources (non-biological only) in urban and rural environments and quantify their potential for enhancing the operational capabilities of small unmanned systems. Energy sources for scavenging are classified into one of the five categories: photonic; kinetic; thermal; electromagnetic; autophagous (self-consuming) structure–power. Photonic sources include the sun and artificial lighting. Kinetic sources include wind, flowing water, and vibrational or oscillatory motion generated on or near moving structures or machinery. Thermal energy sources include objects heated by the sun, ambient air, ground terrain, utility piping, exhaust vents, and chimneys. Electromagnetic energy is available in the form of oscillating magnetic fields surrounding AC power lines. Autophagous structure–power is a multifunctional concept that involves the

* Corresponding author. Tel.: +1 202 404 8324; fax: +1 202 404 7176.
E-mail addresses: james.p.thomas@nrl.navy.mil (J.P. Thomas), muhammad.qidwai@nrl.navy.mil (M.A. Qidwai), james.kellogg@nrl.navy.mil (J.C. Kellogg).

[1] We use the term "energy scavenging" rather than "energy harvesting" to describe overt or covert collection of energy on a small-scale, from natural or artificial sources that are either renewable or non-renewable.

0378-7753/$ – see front matter © 2006 Elsevier B.V. All rights reserved.
doi:10.1016/j.jpowsour.2005.12.084

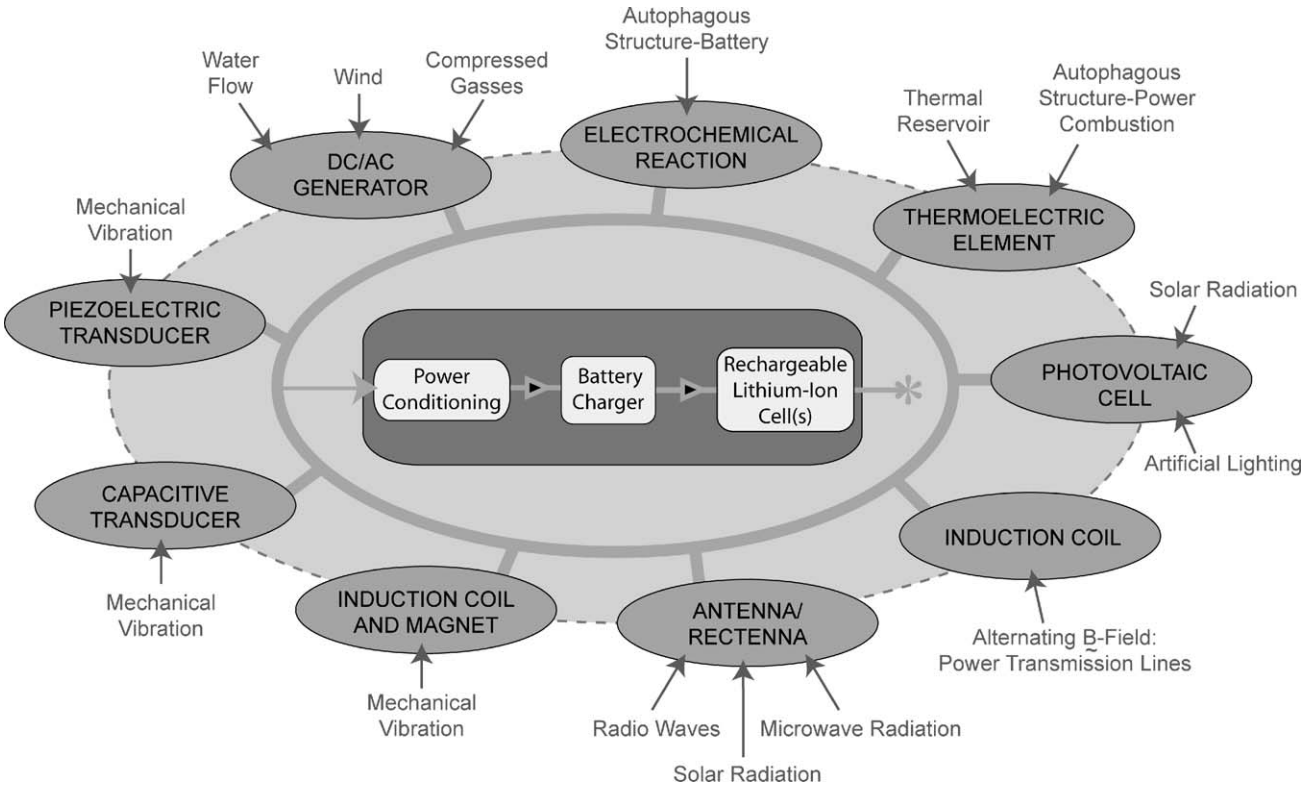

Fig. 1. Various scavengable energies (non-biological) that can be converted into electrical energy for use by small electric unmanned systems.

"transformation" of mechanical structure into an "internal" source of energy.

We assume that the unmanned systems of interest use a rechargeable battery as the primary system energy supply, and that energy scavenged from the environment is used for supplementing and recharging the battery. Identification and implementation of a viable energy scavenging strategy will depend on the system's power requirements, weight and/or size limitations, and operational environment. Energy scavenging options are best considered during the initial design phase of the unmanned system where availability of particular sources of energy in the operational environment can be matched to mission requirements for endurance, mobility, etc. with minimal constraints on the scavenging sub-system mass, size, and implementation. Multifunctional design, in the context of this work, seeks reductions in system weight through replacement of parasitic system structure with load-bearing components of the energy scavenging system (see, for example, Refs. [1–3]).

Energy scavenging devices generally consist of: energy collection elements, conversion hardware, and conditioning/process control electronics (Fig. 1). Power output per unit mass or volume is a key performance metric for the collection elements. The scavenged power must be converted to electricity and conditioned to an appropriate form for charging the system batteries. Impedance load matching between the collectors and storage elements is necessary to maximize the scavenged power. Appropriate electronic circuitry for power conditioning and impedance load matching may be available commercially or may require custom design and fabrication.

Energy from solar, wind, and water sources are commonly "harvested" using large-scale devices [4]. Much less attention has been paid to small-scale energy scavenging methods and devices. A significant portion of the literature focusing on small-scale energy scavenging or harvesting deals with the extraction of energy from kinetic motion. The recent book by Roundy et al. [5] provides a comprehensive examination of vibration energy scavenging for sensor network systems (also see [6–8]). Taylor et al. [9] describe an electrostrictive polymer "eel" that extracts energy from oscillating water flows that are generated downstream from a blunt body in the flow. Piezoelectric generators in shoes [10], textiles [11], and as vibration-based microgenerator devices [12,13] have been considered for energy scavenging. Pescovitz [14] and Chevalier [15] describe efforts to shrink the size of various types of power sources and to use energy scavenging in consumer electronics. MEMS-scale power sources and energy harvesting are considered in Refs. [16–18]. Additional references can be found on the web.[2]

In the area of thermal energy harvesting, Stevens [19] and Lawrence and Snyder [20] consider different aspects of system design for thermal energy scavenging via thermoelectric conversion that exploits the natural temperature difference between the ground and air. Jung et al. [21] have considered thermoelectric power generation from body heat for electronic systems

[2] As of December 2005, the following web-sites with useful energy harvesting information and references were available: http://energyscavenging.anu.edu.au/ and http://www.ife.ee.ethz.ch/~tvonbuer/myindex.html.

embedded in clothing. Fleming et al. [22] examine the use of thermoelectrics for generating electricity from the high temperature exhaust of internal combustion engine propulsion units on unmanned air vehicles.

In this paper, we focus on small-scale energy scavenging from non-biological sources excluding vibrational energy scavenging which is already well documented in the literature. We begin with a description of energy scavenging concepts and notional designs for each of the five energy types: photonic, kinetic-flow, thermal, electromagnetic, and autophagous structure–power. We will show that solar collectors (photonic energy) and autophagous structure–power are capable of supplying power at moderate levels (∼1 to 10 W); thermoelectric generators (thermal energy) and small wind generators (kinetic-flow energy) at low levels (∼10^{-2} to 1 W), and induction antennas (electromagnetic energy) at low to potentially large levels (∼10^{-3} to tens of watts). The proposed concepts and notional designs are compared in several performance areas, and an analysis of photonic scavenging for extending the flight endurance time of electric unmanned air vehicles is provided as an example of using a quantitative system metric to determine requirements on the scavenging hardware.

2. Energy scavenging concepts

2.1. Photonic energy harvesting

Photonic energy (photon radiation) is readily available outdoors (solar radiation; see Fig. 2) and in artificially lighted indoor locations. Approximately 1000 W m^{-2} of solar power is incident on surfaces directly facing the sun on a bright sunny day [23]. Photonic energy can be converted directly to electricity using photovoltaic (solar) cells made from semiconductor materials. Solar cell arrays or panels may also be integrated as multifunctional structural skin in order to provide some load-carrying capacity, which allows for a reduction in structural mass.

A solar cell is basically a semiconductor diode with a large p–n junction in the plane of the cell that is positioned close to the top surface. An electric potential develops between the p- and n-type materials when their junction is exposed to photon radiation. A typical cell can supply current at voltages up to approximately one-half a volt. At lower voltages, the current is nearly independent of voltage but varies with solar radiation intensity. Characteristic current versus voltage (*I–V*) performance for p–n type solar cells is shown in Fig. 3. The short-circuit current, I_{sc}, and the open-circuit voltage, V_{oc}, are two defining characteristics of a solar cell. Together with maximum cell output power, P_{max}, they are used to define the fill factor, FF [24]:

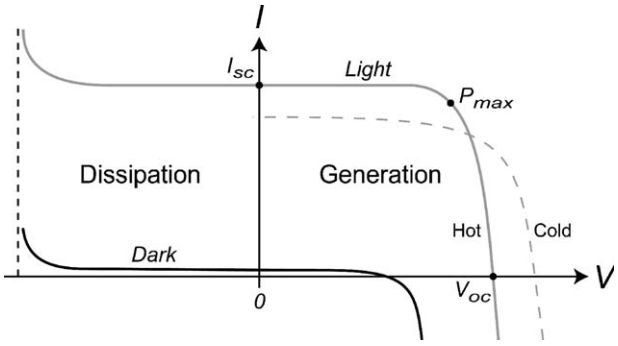

Fig. 3. Current–voltage behavior of silicon photovoltaic cells with (light) and without (dark) incident radiation. Decreasing cell temperature lowers the short-circuit current, I_{sc}, and increases the open-circuit voltage, V_{oc}, leading to a net increase in output power.

$$\mathrm{FF} := \frac{P_{max}}{I_{sc} V_{oc}} \quad (1)$$

The fill factor is a measure of cell quality ranging from 0 (poor) to 100% (excellent). Values in the range of 70–80% are common for commercial cells (see Table 1).

A typical (large-scale) solar power generation system consists of a solar cell array (collector), blocking diodes, a peak power controller to maintain the output current and voltage at maximum power output level (i.e., the knee of the *I–V* curve), and optional sun tracking controls. Blocking diodes and fuses are incorporated to prevent discharge of the battery when the solar panel is not illuminated and to protect against large currents that can develop under ground-faulting conditions [25]. Sun tracking controls ensure that the solar array is oriented perpendicular to the sun's rays to maximize the direct radiation exposure from the sun.

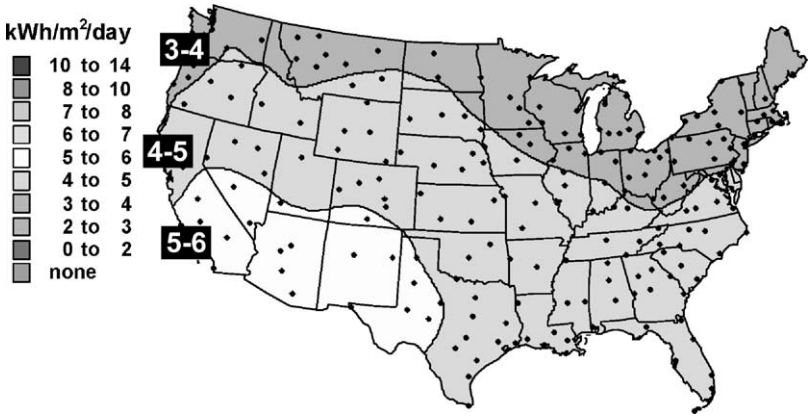

Fig. 2. Daily incident solar radiation averaged over the year for the continental USA [4].

Table 1
Manufacturer specifications for several photovoltaic cells with 1000 W m^{-2} incident radiation

Cell	Dimensions (cm^2)	Thickness (μm)	Weight (g)	V_{oc} (V)	I_{sc} (A)	FF	Efficiency (%)	Power density (W m^{-2})	Specific power (W kg^{-1})
Schott® EFG 1030	100	330	8.2	0.595	3.15	0.77	14.5	145	176
Photowatt® Af	102	300 ± 50	NA	0.606	3.57	0.73	15.4	155	NA
SunPower® A-300	156	270 ± 40	12.5	0.670	5.9	0.78	21.5	195	247
SunPower® Pegasus	21.9	160	0.88	0.680	0.88	0.82	22.5	225	558
Spectrolab® UTJ[a]	32	140	2.7	2.660	0.41	0.83	28.3	285	338

V_{oc} is the open-circuit voltage, I_{sc} the short-circuit current, and FF is the fill factor.
[a] Ultra triple junction ($GaInP_2$/GaAs/Ge); I_{sc} has been scaled by 1/1.353 to correspond with 1000 W m^{-2} incident radiation instead of the quoted value of 1353 W m^{-2}.

The efficiency of conversion from photonic to electrical energy is practically constant over a wide range of incident radiation. Commercial solar conversion efficiencies range from a low of approximately 8% to state-of-art values of 30% or more [26]; some experimental technologies reach as high as 35%. The most common material used in photovoltaic cells is crystalline silicon (c-Si) in single crystal, polycrystal, ribbon and sheet, and thin-layer forms. Efficiencies range from 10% to 23% in state-of-the-art cells. Other solar technologies include the high efficiency multi-junction devices, which stack different photovoltaic cells on top of each other to maximize the capture of incident radiation, and thin film solar cells.

Specifications for several commercial cells including a high-performance triple-junction cell are listed in Table 1. The last two columns show calculated power densities (W m^{-2}) and specific powers (W kg^{-1}), useful cell metrics for scavenger performance evaluation and design calculations. The single-junction modules are roughly equivalent in their power density levels. The triple-junction cell has a larger power density, but these cells cost significantly more than basic single-junction modules. Flexible solar cells with thin-metal foil substrates and efficiencies in the 10–11% range are being used to create portable solar "blanket" generators [27] for military and commercial applications. The cells are embedded in a polymer laminate overcoat for handling and protection against atmospheric degradation. The single- and triple-junction commercial cells are relatively brittle and must be protected from impacts and excessive bending. The flexible cells, on the other hand, can accommodate large bending strains and can be more easily integrated as a multifunctional "power-skin."

Important factors in the design of a solar scavenging system are the radiation intensity and ambient temperature at the collection site, the incident angle of radiation, and load matching for maximum power output. The current and voltage characteristics of the solar collector must be properly matched with the system load in order to maximize the power output and energy collection capability. The "knee" voltage (maximum power output point) depends on the number of cells connected in series and their temperature. The total output current can be increased by adding cells in parallel. Lower temperatures shift the *I–V* curve to lower I_{sc} and higher V_{oc} values producing an increase in the output power (see Fig. 3). Patel [23] (Section 8.6.4) derives an estimate of 0.45% power output decrease for every 1 °C increase in temperature above some reference temperature for typical single crystal Si cells.

Radiation intensity and incident angle affect the output current. Intensity is dependent on weather patterns, and probabilistic weather fluctuations need to be included to accurately predict power output at a fixed location over long durations of time. The incident solar radiation on a flat-plate collector (I_t) is composed of direct beam radiation (I_b), diffuse radiation from the surroundings (I_d), and reflected radiation from nearby surfaces (I_r) [28]:

$$I_t = I_b \cos\theta + I_d + I_r \quad (2)$$

where θ is the angle of incidence (see Fig. 4). Direct beam radiation is the largest component, which makes the angle of incidence a key parameter in solar power collection. The incident radiation on a flat plate collector depends on positioning (inclination and orientation) of the collector and on the motion of the sun during the day and through the year [29]. To maximize the radiation exposure, one must ensure that the angle of incidence remains close to zero at all times. Two collection strategies are typically used to achieve this [30]: dynamic tracking of the sun using a tilted collector, and/or focusing lenses and collector shape variations (e.g., concentrating parabolic collectors). Dynamic tracking is performed in one-axis, east-to-west during

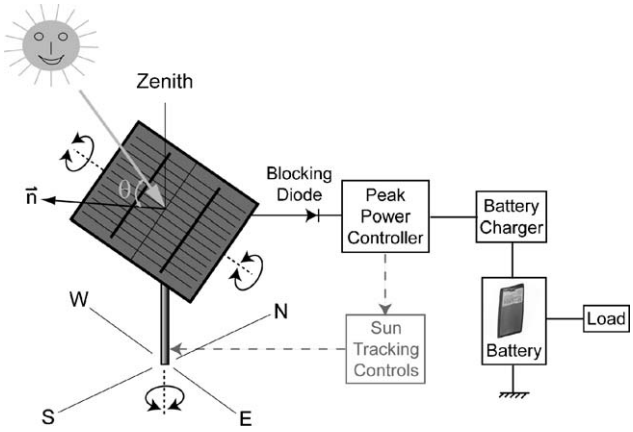

Fig. 4. Typical solar generation system. Major components include the solar collectors, blocking diode, peak power controller and (optional) sun tracking controls.

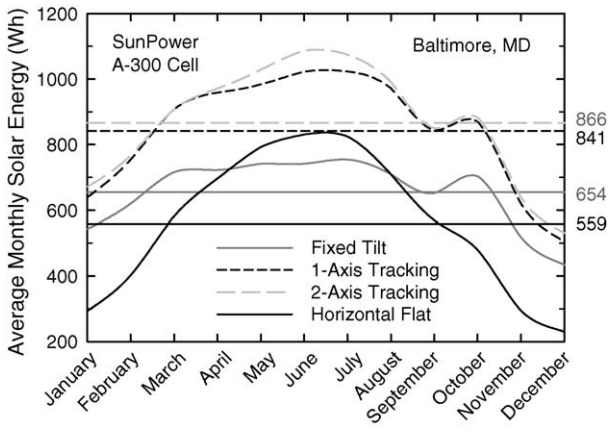

Fig. 5. Average monthly collected energy for four configurations of a SunPower® A-300 solar cell (125 mm × 125 mm) located in Baltimore, MD. The horizontal lines are an overall average of the monthly data. The data for the plots are obtained using manufacturer specifications and the solar calculation program PVWATTS [31].

the day, or two-axes, east-to-west during the day and high-to-low tilt from winter to summer.

We have used a web-based solar analysis tool PVWATTS [31] to estimate the average monthly energy that can be collected by a single SunPower® A-300 photovoltaic cell (Table 1) in the city of Baltimore, MD (latitude: 39.18°N, longitude: 76.67°W, elevation: 47 m). The data plotted in Fig. 5 correspond to PVWATTS output that has been adjusted to account for differences between the A-300 cell and a 1 kW solar panel with default settings.[3] Four configurations are considered: horizontal flat (parallel to the ground), fixed tilt (south facing with an inclination angle of 39.18°), one-axis tracking at an inclination angle of 39.18°, and two-axes tracking. The average monthly energies for each configuration are: 560 Wh for horizontal flat, 655 Wh for the fixed tilt, 840 Wh for one-axis tracking, and 865 Wh for two-axes tracking. As expected, tracking yields better energy scavenging performance, but at the expense of added weight, complexity, and cost of the tracking control equipment. The horizontal collector is more effective at collecting solar energy in the peak summer months than the fixed-tilt collector because the incidence angle is smaller on the horizontal collector at summer solstice.

Solar panel sizing, power electronics control, and multifunctional structure–power implementation are key implementation issues for photonic energy scavenging.

2.2. Scavenging of kinetic-flow energy

Kinetic-flow energy can be found in natural and man-made environments in the form of wind and water currents, and gas or liquid flows in pipes and ducts. The technological concepts and design issues associated with energy scavenging at a "small-scale" from the wind or from flowing water are similar; we focus here on energy scavenging from the wind.

Table 2
Friction coefficients for the wind speed versus height relationship [23]

Terrain type	Friction coefficient, α
Lake, ocean, and smooth hard ground	0.10
Grass one foot in height on level ground	0.15
Tall crops, hedges, and shrubs	0.20
Wooded country with many trees	0.25
Small town with some shrubs and trees	0.30
City area with tall buildings	0.40

Fig. 6 shows that average wind speeds within the continental USA range from 0 to 10 m s^{-1} measured 10 m above the ground. The wind velocity decreases from its free-stream value high above the ground to zero at ground-level, more or less slowly depending on the roughness of the terrain. An approximate expression for the mean flow velocity, V_h, at height h above "rough" ground is given by [23,32]:

$$V_h = V_{\text{ref}}\left(\frac{h}{h_{\text{ref}}}\right)^{\alpha} \tag{3}$$

where V_{ref} is the wind speed at height h_{ref}, and the exponent α accounts for terrain roughness effects. Empirical values for α for different terrains are given in Table 2.

The power available from wind flow equals the rate of flow of kinetic energy per second:

$$P_{\text{wind}} = \frac{1}{2}\frac{\mathrm{d}m}{\mathrm{d}t}V^2 = \frac{\rho A V^3}{2} \tag{4}$$

where ρ is the air density, A the cross-sectional area of flow, and V is the upstream wind velocity. This relationship is plotted in Fig. 7, which shows wind power versus flow area for various wind speeds.

The flow of wind can be converted into a shaft rotation through the use of a rotor, which is composed of one or more airfoil blades that rotate with the shaft. The rotor transforms the kinetic wind power into rotational shaft power using aerodynamic lift and drag forces created on the rotor blades by the wind flow to produce shaft torque. The amount of power extracted from the wind flow equals the difference in upstream and downstream wind powers [23,32]:

$$P_{\text{shaft}} = \frac{1}{2}\frac{\mathrm{d}m}{\mathrm{d}t}(V^2 - V_{\text{down}}^2) \tag{5}$$

The mass flow rate is calculated using the average wind velocity:

$$\frac{\mathrm{d}m}{\mathrm{d}t} = \rho A\frac{V + V_{\text{down}}}{2} \tag{6}$$

resulting in a shaft power:

$$P_{\text{shaft}} = \frac{\left(1 + \frac{V_{\text{down}}}{V}\right)\left[1 - \left(\frac{V_{\text{down}}}{V}\right)^2\right]}{2}\frac{\rho A V^3}{2} = C_{\text{p}}P_{\text{wind}} \tag{7}$$

[3] PVWATTS output is multiplied by (3.04 W × 0.86 × 0.215)/(1000 W × 0.77 × 0.114) where 3.04 W corresponds to the A-300 cell rating, 1.0 kW to default PVWATTS panel rating, 0.86 to the A-300 derate factor (0.95 manufacturer, 0.98 mismatch, 0.995 diodes, 0.98 wiring, and 0.95 soiling), 0.77 to the default derate factor, and 0.215 to the A-300 efficiency, 0.114 to the default efficiency.

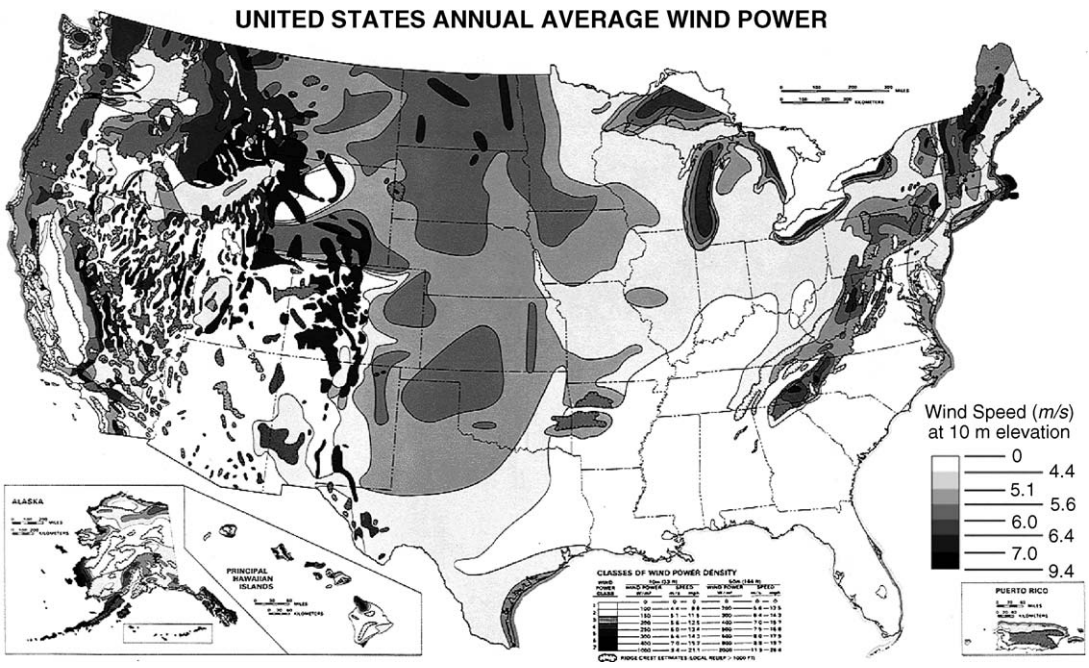

Fig. 6. Average wind speed (power density) in the USA [4].

with the rotor power coefficient C_p given explicitly by

$$C_p := \frac{\left(1 + \frac{V_{down}}{V}\right)\left[1 - \left(\frac{V_{down}}{V}\right)^2\right]}{2} \quad (8)$$

C_p is the fraction of upstream power captured by the rotor blades; it has a maximum value of 0.593 when V_{down}/V equals one-third.

Numerous rotor blade configurations have been used or suggested for use in windmill and wind-powered machinery. Chapter 3 on wind-blade taxonomy in [33] divides rotors into two primary types: horizontal and vertical. Horizontal configurations include common two and three blade propeller designs used on modern large-scale windmills for electrical energy production and airplane propellers, and the classic four-blade Dutch and multiblade American windmill designs. These configurations must be oriented into the direction of wind flow in order to operate efficiently. Vertical rotor configurations include turbines and Darrieus designs that use aerodynamic lift forces on the rotor blades to produce rotation, and Savonius designs that use drag to produce rotation. Vertical rotors operate efficiently for all horizontal wind flow directions, an important advantage that can greatly simplify the energy scavenging device design. The swept area of the rotor is much larger than the combined area of the blades. The ratio of blade area to swept area is called the "solidity", and the solidity of modern two and three blade horizontal rotor designs is 5–10% for wind applications [23]. Rotor starting torque increases and rotation speed decreases as solidity increases. The efficiency, C_p, of various rotor types is plotted in Fig. 8 as a function of the ratio of rotor blade tip speed to upstream wind velocity. These curves are based on fluid flow analyses for each of the rotor types [32], and the upper bound on performance for all types of rotors is the 0.59 value obtained from Eq. (8). In Fig. 8, blade tip speed is defined as $V_{tip} = r\omega$, where r is the rotor radius and ω is the rotation velocity in rad s^{-1}.

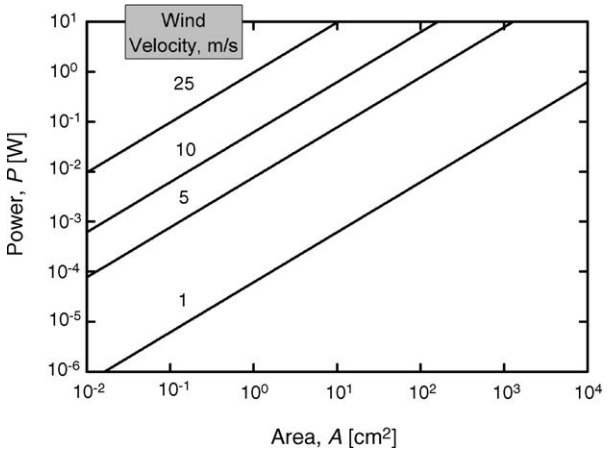

Fig. 7. Kinetic-flow power of wind as a function of the flow cross-section area at various wind speeds.

The rotor transforms the kinetic-flow energy from the wind into shaft power. An electric generator is needed to transform the rotational shaft power into useable electrical energy for the unmanned system. Small electrical "RC-hobby" motors can be used to generate electric power by mechanically driving their shaft in rotation. They generally exhibit efficiencies greater than 60% in converting electrical power to shaft rotation power (motor operation) with typical rotation speeds in the thousands to tens of thousands of revolutions-per-minute (rpm). They are configured in applications as either direct-drive, low-torque–high-RPM motors or as gear-drive, high-torque–low-RPM motors.

In order to assess the potential of small RC-hobby motors as electrical generators, we have tested several common RC aircraft motors to characterize their output voltage, current, power,

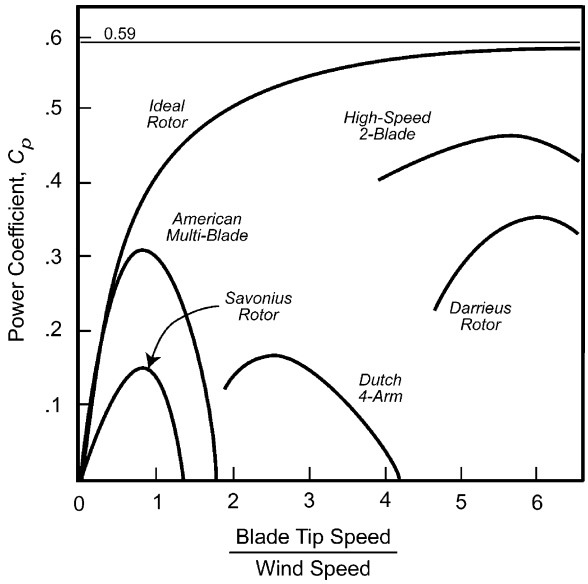

Fig. 8. Power coefficients (shaft output power over wind input power) for several rotors as a function of the ratio of blade tip speed to wind speed (after Ref. [33]).

and conversion efficiency as a function of output load resistance and the shaft input rotation speed and torque. Data for two such motors is shown in Fig. 9. The low conversion efficiencies (less than 60%), particularly at low input RPM levels, is the most relevant characteristic for the energy scavenging application. These two brush-type motors are typically operated well above 10,000 rpm, which explains, in part, why they do not perform well as a low RPM generator. A gearbox can be used to increase the input rotation speed, but a higher corresponding rotor torque would be required. We believe that significant improvement in generator performance is possible using a customized motor–generator design with control over the field and armature windings, timing, etc. Ultimately, the motor–generator and gearbox (if required) would have to be matched to the wind rotor and its operational environment to optimize the power scavenging capability of this type of system.

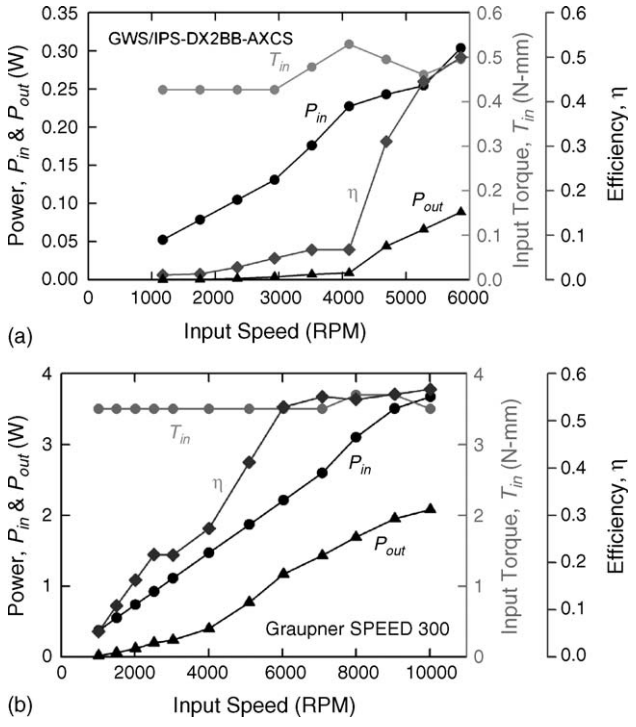

Fig. 9. Electrical power generation performance for two DC hobby aircraft motors. The GWS motor–gearbox (a) is ∼23 mm diameter, 46 mm length, and 26 g mass. The Graupner motor (b) is ∼24 mm diameter, 31 mm length, and 50 g mass.

To explore the notion of wind-energy scavenging a bit further, consider a wind-generator design that uses a vertical Darrieus (egg-beater) rotor to achieve efficient (C_p = 23–35% from Fig. 8) energy extraction from wind flowing in any direction. A Darrieus rotor constructed using adjustable elastic buckling airfoil blades would allow for compact rotor stowage when not in use and field adjustment to changing wind speeds to achieve optimal performance. Assume that the rotor is located ∼0.25 m above smooth hard ground, and that the average wind speed at the rotor centroid is 5 m s^{-1} (11.2 mph) corresponding to an ambient wind velocity of 7.2 m s^{-1} at 10 m elevation using Eq. (3) and $\alpha = 0.1$ from Table 2.

The swept area of a Darrieus rotor can be approximated by that of an ellipse:

$$A = \pi \frac{(W_{\text{rotor}})_{\max}}{2} \frac{h_{\text{rotor}}}{2} \tag{9}$$

If the maximum width of the rotor $(W_{\text{rotor}})_{\max}$, is 10 cm and the height of the rotor, h_{rotor}, is 15 cm, then the total swept area of the rotor is 118 cm^2. According to Eq. (4) or Fig. 7, ∼0.9 W of wind power will be available at the rotor. This translates into 0.27 W of shaft power assuming a rotor efficiency of 30%. The tip-to-wind speed ratio is ∼5.0 at 30% efficiency (Fig. 8), from which we can calculate a rotor rotational speed of 4800 rpm and torque of 0.5 N mm for driving the motor–generator. Based on the available rotor torque, we can see that the GWS/IPS-DX2BB-AXCS motor-generator in Fig. 9a would be appropriate, and that using this motor–generator would result in ∼50 mW of electrical power being scavenged from the wind. This corresponds to an overall efficiency of ∼6% or 4.2 W m^{-2} from wind power to electrical power. These efficiency and power density values are low relative to the 200–500 W m^{-2} performance numbers quoted in [23] for 10–40 m diameter wind machines.

Clearly, more work on small-scale wind generator systems needs to be performed before the feasibility, performance levels, and viable implementations for specific unmanned system applications can be definitively ascertained. Achieving good power generation performance from small motors, rotor design for efficiency and stowage, and minimizing component weights are the key implementation issues.

2.3. Thermal energy scavenging

A temperature differential is necessary to transfer or extract energy from a thermal reservoir. Low-grade heat manifested by "small" temperature differences between various objects (natural and industrial) within the environment is freely available. Benson and Jayadev [34] cite temperature differentials for the

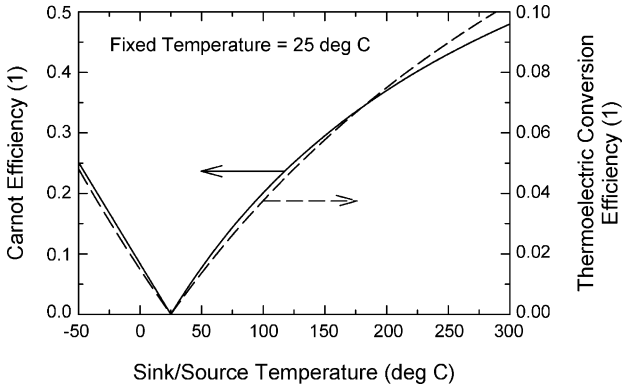

Fig. 10. Carnot efficiency for a heat-engine and the thermoelectric conversion efficiency ($ZT_m \sim 1$) as a function of temperature and one thermal reservoir held constant at 25 °C.

following sources: 80–180 °C for geothermal steam, 15–20 °C for thermoclines within the Gulf of Mexico and hydroelectric reservoirs, ~75 °C from solar ponds, 15 °C from the waste heat generated by power plants, and as much as 75 °C from industrial waste heat sources. Stevens [19] and Lawrence and Snyder [20] consider thermoelectric energy scavenging methods that use the small temperature differential (<1 °C) between sub-surface soil and ambient air; Matsuura and Rowe [35] discuss these and other sources of low-grade heat. Small to moderate temperature differentials can also be found between ambient air and urban heat sources like exhaust stacks and vents, steam lines, industrial motors and equipment, and exhaust and cooling systems on various types of powered vehicles.

Heat engines convert thermal energy into mechanical work. The Carnot equation for the maximum theoretical efficiency of a heat engine connected to thermal reservoirs maintained at hot, T_H, and cold, T_C, temperatures:

$$\eta_{Carnot} = \frac{T_H - T_C}{T_H} \tag{10}$$

is founded on the first and second laws of thermodynamics and serves as a "Gold Standard" for thermal-to-electric energy conversion. Fig. 10 plots the Carnot efficiency as a function of temperature with one thermal reservoir temperature (either T_C or T_H) held fixed at 25 °C. The significant characteristic to note about this plot is the low efficiency for small to modest temperature differences: 3% at $\Delta T = 10$ °C; 14% at $\Delta T = 50$ °C; only 40% at $\Delta T = 200$ °C.

There are several processes that can create electrical current from a thermal gradient [36]: thermoelectric, thermionic, thermomagnetism, ferroelectricity, and the Nernst effect. Thermoelectric conversion is the most effective of these processes and is considered in more detail below. Thermionic generation works by using heat to liberate electrons on the cathode and condensing them on a cooled anode. Thermomagnetic and ferroelectric processes use the large change in magnetic permeability or dielectric constant with temperature, and subsequent change in stored inductive or electrostatic energy, to generate electrical power from cyclic temperature sources. Nernst-effect generators use the electromotive force that develops along the length of a semiconductor material when a heat flux flows across lines of magnetic force, both of which are perpendicular to the semiconductor axis and to each other.

Thermoelectric conversion works through the absorption and liberation of heat at the connection interface between compositionally distinct electrical conductors (thermocouple) with a flowing current (Peltier effect). The electric current is generated by a voltage difference that is created within each conducting leg when subjected to a temperature gradient along the length of the leg (Seebeck and Thompson effects). Thermoelectric modules are composed of alternating arrays of n- and p-type semiconductor elements connected electrically in series and thermally in parallel (Fig. 11). The interfaces between the n- and p-type semiconductor materials on the hot and cold sides of the thermoelectric module form a series of connected thermocouples that give rise to a module voltage equal to the sum of the individual thermocouple voltages and a module current equal to the smallest individual thermocouple current.

Three semiconductor materials, each corresponding to a different maximum temperature, are commonly utilized in thermoelectric devices [37]:

- bismuth–telluride: highest Z but limited to $T < 250$ °C;
- lead–telluride: next highest Z and limited to $T < 500$ °C;
- silicon–germanium: lowest Z but can operate up to $T \sim 1000$ °C.

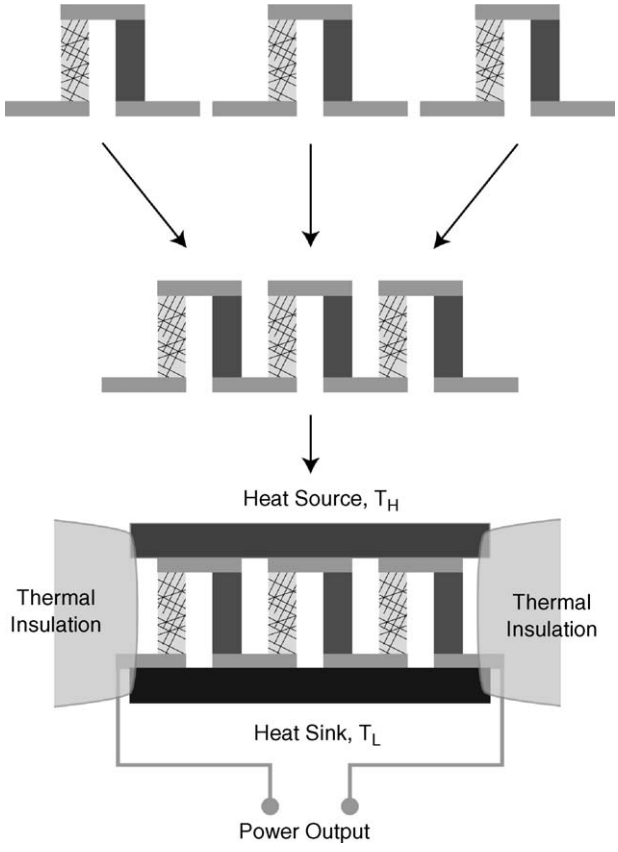

Fig. 11. Thermoelectric generator composed of alternating p- and n-type semiconductor thermocouples arranged electrically in series and thermally in parallel. Heat flow from the source to the sink produces electrical power at the output leads (after Ref. [37]).

Table 3
Manufacturer specifications[a] and calculated performance (three right columns) for three thermoelectric modules

Manufacturer (model no.)	Dimensions (mm)	Weight (g)	T_H and T_C (°C)	Power (W)	Voltage (V)	T_E efficiency, η_{TE} (%)	Specific power (W kg^{-1})	T_E efficiency, $\eta_{TE}(100, 20)$ (%)	Power, $P(100, 20)$ (mW)
Hi-Z (HZ-2)	29 × 29 × 5.1	13.5	230, 30	2.5	3.3	4.5	185	0.53	300
Kryotherm (TGM-127-1.0-1.3)	30 × 30 × 3.6	10.5	150, 50	1.9	2.6	3.8	180	0.97	485
Tellurex (CZ1-1.0-127-1.27 HT)	34 × 31 × 3.3	7.5	175, 50	2.5	3.5	4.5 (est)	330	0.92	500

T_H and T_C denote the hot- and cold-side temperatures, respectively.
[a] Data obtained from: http://www.hi-z.com; http://www.kryothermusa.com; http://www.tellurex.com.

Z is a "Figure-of-Merit" quantity for the thermocouples used in thermoelectric cooling and power generation and is defined as [38]:

$$Z = \frac{(\alpha_p - \alpha_n)^2}{KR} \tag{11}$$

where α_p and α_n are the absolute Seebeck coefficients for the 'p' and 'n' semiconductor legs of a module's thermocouples, K the thermal conductivity of the 'p' and 'n' legs in parallel, and R is the electrical resistance of the 'p' and 'n' legs in series:

$$K = \frac{\lambda_p A_p}{L_p} + \frac{\lambda_n A_n}{L_n} \quad \text{and} \quad R = \frac{L_p \rho_p}{A_p} + \frac{L_n \rho_n}{A_n} \tag{12}$$

In Eq. (12), $\lambda_{p,n}$ is the thermal conductivity, $\rho_{p,n}$ the electrical conductivity, and $L_{p,n}$ and $A_{p,n}$ are the length and cross-section area of the 'p' and 'n' thermocouple materials. Larger values of Z indicate increasing reversible thermoelectric effects over irreversible (efficiency decreasing) heat transfer and electrical (Joule resistance) energy dissipation effects.

For thermoelectric generation, the following efficiency factor is used [38]:

$$\eta_{\text{thermoelectric}} = \eta_{\text{Carnot}} \frac{M - 1}{M + T_C/T_H} \tag{13}$$

where $M = (1 + ZT_m)^{1/2}$ and $T_m = (T_H + T_C)/2$ is the mean temperature. All three of the thermoelectric materials mentioned above have $ZT_m \sim 1$ when operating close to their maximum temperature limit. Taking $ZT_m \sim 1$ and $T_C = 293$ K in Eq. (13) results in a thermoelectric conversion efficiency that is 17–25% of the Carnot efficiency for all $T_H > T_C$ (Fig. 10).

Rowe and Min [39] describe several useful metrics for assessing thermoelectric power generation. Two key ones are power output (per unit mass or volume) as a function of hot and cold temperature difference, and conversion efficiency, which is defined as the ratio of electric output power to heat input power (i.e., thermal energy flow rate through the module). Improvements in thermoelectric efficiency are being sought through materials research and thermocouple design to increase ZT_m and engineering efforts to shrink the size and weight of the module assembly to maximize output power per unit volume and mass.

A variety of thermoelectric modules are available commercially, but most are optimized for cooling rather than power generation. Table 3 lists manufacturer data for several commercial thermoelectric generator modules. In order to directly compare the modules, we have calculated module efficiency and power output estimates for $T_H = 100$ °C and $T_C = 20$ °C. Z estimates for each module are calculated using Eqs. (13) and (10) with reported module efficiency and high/low temperature data. These Z estimates are then used in Eq. (13) to calculate conversion efficiencies at $T_H = 100$ °C and $T_C = 20$ °C (i.e., $\eta_{TE}(100, 20)$). Power output at $T_H = 100$ °C and $T_C = 20$ °C is calculated by scaling the reported specific power values by $\eta_{TE}(100, 20)/\eta_{TE}$ and then multiplying by the module weight. Table 3 shows optimal module efficiencies in the range of 4–5% when operated at their high temperature limit values. The estimated conversion efficiency drops-off to less than 1% and the power output level to less than half-a-watt per module when $T_H = 100$ °C and $T_C = 20$ °C.

A thermal energy scavenging system requires one or more thermoelectric modules, heat exchangers on the hot and cold sides of the module, mechanical structure for clamping the heat exchangers to the module and ensuring good thermal contact, thermal insulation to prevent heat losses through the sides, and power electronics for impedance load matching. The heat exchangers should be designed to maximize the heat transfer rate through the module, from the high to low temperature side, while minimizing mass and volume/size. Thermal resistance at the heat exchanger/module interfaces must be minimized through (optimally) direct atomic bonding or through clamping at moderate pressures with polished interface surfaces coated with a thin, highly conductive, conformal layer (e.g., thermal grease).

The key implementation issues for thermal energy scavenging are related to maximizing thermal performance of the heat exchangers and reducing mass of the heat exchangers and thermoelectric module(s) attachment hardware.

2.4. Electromagnetic (EM) energy scavenging

Radio, television, and microwave communications, visible light, X-rays, etc., are forms of electromagnetic (EM) radiation distinguished by their location in the frequency spectrum. For example: 3 kHz–300 GHz is used for AM, FM, and microwave radio communications, 300 GHz to 10^{15} Hz denotes infrared and visible light; $>10^{15}$ Hz denotes ultraviolet, X-rays, gamma rays, and cosmic rays.

The energy associated with EM radiation can be collected for use by an appropriately designed antenna and power conditioning circuitry. Berland et al. [40,41] describe an antenna that

converts solar radiation in the THz frequency range directly into DC power. Such devices are called "rectennas", and they consist of an antenna tuned to absorb incident solar radiation coupled with high-frequency–response tunneling diodes to rectify the collected AC signal into DC power. They report conversion efficiencies greater than 85% for incident monochromatic radiation in the radio frequency range, in agreement with model predictions made by Corkish et al. [42]. Conversion of incident solar energy to DC power has not yet been demonstrated due to the need for suitable diodes with low losses at the higher frequency range of visible light.

Energy is also present in the magnetic fields that radiate from wires and conduit passing an alternating current (AC). Magnetically linking a wire coil "induction antenna" to this oscillating magnetic field provides a means for scavenging energy. An induction antenna effectively functions as a current (instrument) transformer when the wire coil encircles the radiating conductor and as an "air-gap" transformer when placed in proximity to the conductor. An unmanned system can scavenge energy by latching onto an AC power line with induction "talons" or by simply locating in close proximity to an AC conductor with an appropriately designed air-gap induction antenna(s).

The radiated magnetic field strength, B_s, about a current carrying conductor is given by Ampere's Law:

$$\oint \underset{\sim}{B} \cdot \mathrm{d}\underset{\sim}{l} = \mu_0 I \rightarrow B_s = \frac{\mu_0 I}{2\pi r} \tag{14}$$

where μ_0 is the magnetic permeability constant for air ($4\pi \times 10^{-7}$ W At^{-1} m^{-1}), I the conductor current (A), and r is the distance (m) from the center of the conductor to the point at which B_s is calculated.

Faraday's Law of Induction relates the induced electromotive force (V) across the terminals of a wire coil of N turns (our induction antenna for energy scavenging) to the time rate-of-change of the magnetic flux through the core of the antenna:

$$V = -N\frac{\mathrm{d}\Phi_{\mathrm{core}}}{\mathrm{d}t} \tag{15}$$

The core flux Φ_{core} is related to the magnetic field in the core, B_{core}, by the relation:

$$\Phi_{\mathrm{core}} = \int_{\text{core area}} \underset{\sim}{B}_{\mathrm{core}} \cdot \mathrm{d}\underset{\sim}{S} \tag{16}$$

The magnetic field in the core, B_{core}, is governed by the magnetic properties of the core material (i.e., the magnetization or BH curve; Fig. 12) and the externally imposed magnetization force, H_s, which originates in the AC magnetic field produced by a current carrying conductor. The magnetization force at the core location, assuming an air medium, is given by: $H_s = B_s/\mu_0$. The magnetic field present in the core equals:

$$B_{\mathrm{core}} = \mu_{\mathrm{core}} H_s \tag{17}$$

where $\mu_{\mathrm{core}} = \mu_{\mathrm{core}}(H)$ is the magnetic permeability of the core material defined as the slope of the magnetization curve, $\mathrm{d}B/\mathrm{d}H$, as a function of the magnetization force H (see Fig. 12).

Eq. (16) simplifies to: $\Phi_{\mathrm{core}} = B_{\mathrm{core}} A_{\mathrm{core}}$ when the magnetic flux through the induction coil core of cross-section area A_{core} is uniformly distributed. Using Eq. (14), we can express the core flux as a function of the core material and geometry, the source conductor current, and the distance from the core to the conductor:

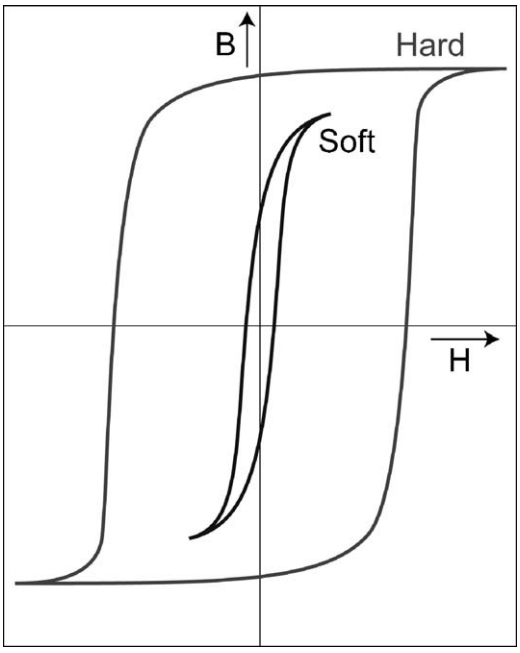

Fig. 12. Magnetization curves for hard (magnets) and soft (transformer cores) ferromagnetic materials. Magnetic permeability, μ, is the slope of B vs. H curve: $B = \mu(H)H$. Induction antennas for scavenging EM energy require the use of soft ferromagnetic material cores.

$$\Phi_{\mathrm{core}} = \frac{\mu_{\mathrm{core}} I}{2\pi r} A_{\mathrm{core}} \tag{18}$$

The root mean square (RMS) power extracted from an induction antenna can be calculated for an assumed sinusoidal AC current in the source conductor. Let $I = I_0 \sin(2\pi ft)$, substitute into Eq. (18), and then use Eq. (15) to calculate the voltage that develops across the induction antenna terminals. For a given induction antenna scavenging system with impedance, Z (coil, load, etc.), the RMS power ($0.707 P_{\max}$) dissipation is given by

$$P_{\mathrm{rms}} = \frac{V_{\mathrm{rms}}^2}{Z} = \frac{N^2 \mu_{\mathrm{core}}^2 f^2 I_{\mathrm{rms}}^2}{Z r^2} A_{\mathrm{core}}^2 \tag{19}$$

where I_{rms} is the RMS current (i.e., $0.707 I_0$). Eq. (19) shows that the power output of the induction antenna is controlled by the design variables: N, μ_{core} and A_{core}; the system impedance, Z; the distance r from antenna to the AC current source; the magnetic field source characteristics: f and I_{rms}.

Power output values have been calculated using Eq. (19) for several notional induction antenna designs with: $A_{\mathrm{core}} = 1\ \mathrm{cm}^2$, $Z = 1\ \Omega$, and $f = 60$ Hz. The results, listed in Table 4, show a large range of power collection capability for the EM induction antenna concept. Design and optimization of the induction scavenging system should be based on expected field strengths at readily approachable distances, coil turns, wire gauge, geometry, core material, etc.

The key implementation challenges for induction energy scavenging are related to antenna design (materials, geometry,

Table 4
Calculated power scavenged from induction antennas assuming: $f = 60$ Hz, $A_{core} = 1$ cm^2, and $Z = 1\ \Omega$

Coil turns N	Core permeability, μ_{core} (W At^{-1} m^{-1})	Distance, r (m)	Current, I (A)	Power, P (W)
1	$4\pi \times 10^{-7}$ (air core)	1	1	5.68×10^{-17}
1	$1000 \times (4\pi \times 10^{-7})$	1	1	5.68×10^{-11}
100	$1000 \times (4\pi \times 10^{-7})$	0.01	100	56.8
100	$1000 \times (4\pi \times 10^{-7})$	0.1	100	0.568
1000	$1000 \times (1\pi \times 10^{-7})$	1	10	0.00568

The first row corresponds to an antenna with an air core and the remaining rows to antennas with a soft ferromagnetic material core.

etc.) for optimal energy collection, given the source characteristics, low mass, and integrating the antenna into the unmanned system's structure to achieve possible multifunctional benefits.

2.5. Autophagous structure–power

Autophagous structure–power refers to system components that are multifunctional in the sense of being able to carrying mechanical loads and provide energy for the system through a "self-consuming" transformation process. The structure and power functions may occur simultaneously, with components that carry mechanical loads while concurrently providing system power, or sequentially, with components that carry mechanical loads for some fixed period of time after which they are consumed to create system power. The potential loss of structural capability and the loss of mass as material is consumed for power must be taken into account in the system/component design. Multi-mode missions with large changes in structural requirements during the course of a mission can take advantage of sequential autophagous structure–power. Examples include: space satellites with large launch loads and much lower orbit loads, or an expendable unmanned air vehicle designed to transport a sensor(s) to a desired location where it lands and serves thereafter as a non-flying platform for sensor power, communications, etc. Launch or flight related structure (e.g., internal struts, wings, empennage, etc.), is not needed in the later phases of the mission, and this structure can be consumed to provide additional system power.

Multifunctional structure–power components can be developed by extracting structure function from an existing energy storage material or by extracting energy from an existing structural material. Fig. 13 shows the energy storage capacity for a variety of solid, liquid, and gaseous hydrocarbon materials and electrochemical battery systems plotted on a per unit mass (specific energy) versus per unit volume (energy density) basis. The battery data other than LiF includes packaging and auxiliary mass (electrolyte, current collection materials, electrodes, etc.) in the energy values while the hydrocarbon fuel, plastic, and LiF battery data pertain only to the active materials. Packaging/auxiliary mass can account for a large fraction (>50%) of total energy system mass, particularly as the size decreases. Solid polymers in the "hydrocarbon" class [43] exhibit higher energy densities and comparable specific energies compared with the conventional liquid and gaseous fuels. Hydrogen has the highest specific energy, but its energy density is lower than most of the other combustible fuels. The LiF couple represents the highest energy possible in a battery system combining the most electropositive element (Li) with the most electronegative element (F) [44]. Battery systems do not store as much energy per unit mass or volume as the combustible hydrocarbons, but they provide energy in a form that can be directly utilized by the electric unmanned system. Hydrocarbons can be used with a solid oxide fuel cell to provide electricity, or they can be combusted to provide large amounts of heat energy. The heat energy must be transformed into electricity using a heat-to-electricity conversion process, but thermoelectric conversion processes are relatively inefficient with a significant fraction of their mass usually taken up by the auxiliary components.

In the following subsection, we will examine an autophagous structure–power system called "GasSpar" that uses the vapor pressure from a two-phase liquid–gas hydrocarbon fuel to provide structural reinforcement of a lightweight inflatable structural beam.

2.5.1. Autophagous GasSpar

The autophagous GasSpar system uses the vapor pressure of butane or propane fuel to stiffen and strengthen an inflatable composite beam [45,46]. The fuel can directly power an internal combustion engine or solid-oxide fuel cell, or it can be combusted and used to create electricity via thermoelectric conversion. A notional GasSpar system for an electric UAV is

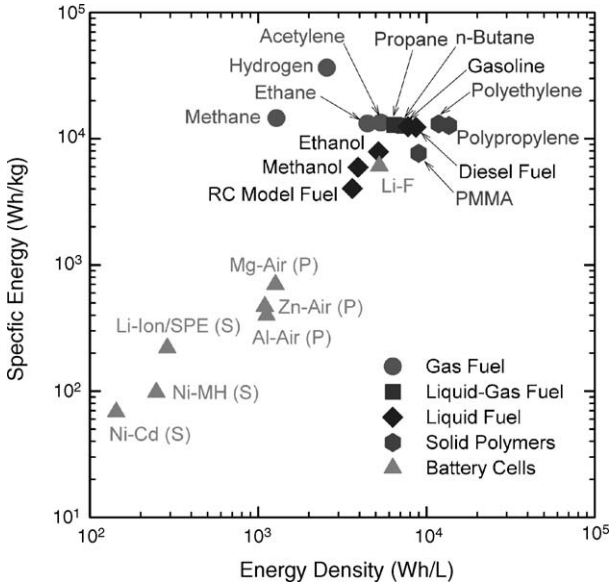

Fig. 13. Energy storage performance for select hydrocarbon fuels and electrochemical cells at room temperature: gaseous, liquid–gas, liquid, and solid fuels and electric batteries.

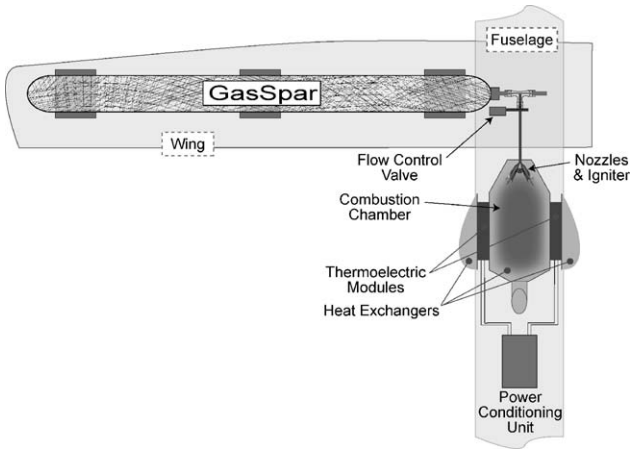

Fig. 14. Notional autophagous structure–power system for an unmanned air vehicle. GasSpar forms the main structural element of the wing, and a combustion thermoelectric conversion process is used to convert the two-phase hydrocarbon fuel stored inside GasSpar into electricity.

shown in Fig. 14. It consists of a GasSpar in the aircraft wing with a converter in the fuselage to burn the fuel and create electric power using thermoelectric Bi_2Te_3 modules. The GasSpar beam is a lightweight, flexible composite shell with an internal polymer fuel "bladder." The butane or propane pressurizes the bladder core, expanding the cross-section to provide bending stiffness and strength. The pressurized fuel replaces the structural core material (typically polymer foam or honeycomb) that would be needed for bending performance.

The pressure of a saturated gas vapor in equilibrium with its liquid phase is dependent on temperature alone. Saturation vapor pressure as a function of temperature for several hydrocarbon fuels is shown in Fig. 15. This pressure remains constant (assuming constant temperature) as long as any liquid phase remains. The constant pressure provided by the liquid–gas equilibrium state of the fuel core provides GasSpar with a constant level of mechanical performance until all of the fuel is consumed.

N-Butane and propane fuels for GasSpar are readily available, have high heats of combustion (~12,800 Wh kg^{-1}), a wide

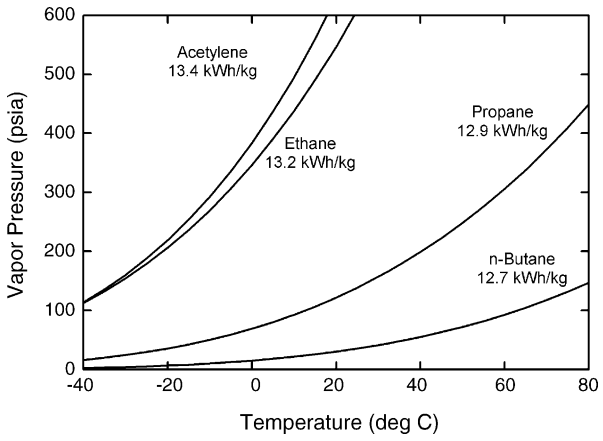

Fig. 15. Vapor pressure–temperature plots for acetylene, ethane, propane, and n-butane; at 20 °C, their vapor pressures are: 610, 520, 125, and 30 psia, respectively. Data from: http://webbook.nist.gov/chemistry/fluid/.

range of vapor pressures, and burn cleanly. They can be mixed to tailor the pressure–temperature curve and achieve the desired mechanical performance over a range of operational temperatures. The power per unit mass of the GasSpar system equals the electrical output power of the thermoelectric generator(s) divided by the total system mass. Specific energy of the GasSpar system is determined by the amount of fuel stored in GasSpar, the efficiency of the combustion and conversion processes, and the total system mass. For the GasSpar autophagous energy system to achieve a specific energy of 200 Wh kg^{-1} and match that of state-of-the-art commercial Li-ion secondary cells, the following conditions must be met:

$$\frac{\text{fuel mass}}{\text{system mass}} \times \frac{\text{thermoelectric input energy}}{\text{theoretical combustion energy}} = \eta_{\text{mass}} \times \eta_{\text{combustion-transfer}} > 37\% \quad (20)$$

The 37% value on the right-hand side is obtained by dividing target performance, 200 Wh kg^{-1}, by the specific energy of *n*-butane (12,800 Wh kg^{-1}), then dividing by 5%, an assumed heat-to-electricity conversion efficiency for the thermoelectric module(s), and then dividing by 85%, an assumed efficiency for DC power conditioning. On the left hand side, the first term accounts for the proportion of GasSpar system mass taken up by the energy producing *n*-butane fuel. The second term accounts for the proportion of theoretical fuel combustion energy that is actually transported through the thermoelectric module(s) for conversion to electricity. The 37% value will be achieved if the individual mass and combustion-transfer factors are each greater than 60%. Increasing GasSpar's fuel storage volume and/or decreasing the thermoelectric combustion-converter weight can be used to increase the fuel mass fraction, and thermal design optimization of the combustion and heat-transfer processes can be used to increase the combustion-transfer efficiency.

A GasSpar system prototype developed at the Naval Research Laboratory [45,46] has demonstrated a 20 Wh kg^{-1} specific energy at 2.9 W kg^{-1} specific power with approximately 7 h of burn time for a total of 8.4 Wh usable electrical energy. The GasSpar beam itself is 1.9 cm in diameter, 46 cm in length, and weighs 46 g empty. Total system mass is 420 g with 303 g of thermoelectric combustion-converter and 70 g of *n*-butane fuel (880 Wh of chemical energy). The core volume of GasSpar is ~130 cm^2, which would be filled with ~7–40 g of polymer foam [47], depending on the structural design requirements.

The overall conversion efficiency of this proof-of-concept prototype is ~1%. The n-butane fuel provides 117 kPa of vapor pressure at room temperature resulting in a measured 2.5-fold increase in bending stiffness and 4.2-fold increase in bend-buckling strength over the unfilled beam. Significant improvements in the overall system efficiency and specific energy and power values can be achieved through design improvements in the hot- and cold-side heat exchangers and burner, and reductions in component weights, especially those associated with the combustion-converter.

Key implementation issues for GasSpar structure–power systems include the design and fabrication of multifunc-

tional structural components that optimally utilize the fuel vapor pressure to achieve mechanical performance and the need for efficient, lightweight chemical-to-electric conversion devices.

3. Discussion

The selection and design of an energy scavenging subsystem should be guided by the improvement it affords in the unmanned system's performance (e.g., endurance time, mobile range, communications range, etc.). To assess a particular design, quantitative models are needed that relate the unmanned system's performance to its energy storage, energy scavenging, and power dissipation (e.g., propulsion, control, sensing, etc.) components and characteristics. Such models can be used for identifying scavenging strategies and then configuring and sizing the energy scavenging and storage components for optimal system performance. An example of this is provided below for solar scavenging on an electric unmanned air vehicle.

The combination of energy storage and energy scavenging devices creates a "hybrid power supply" that can be characterized by a Ragone plot [48] of deliverable energy versus power draw rate, each normalized by mass or volume. Comparatively, energy scavengers are expected to provide "large" amounts of energy at low power levels and the on-board batteries provide "limited" amounts of energy at high power levels. The combination of the two creates a power supply with better Ragone performance (i.e., more energy at higher draw rates) than either of the individuals. Relative sizing of the battery and scavenger provide an energy–power tailoring capability that can be used to optimize system performance.

Every unmanned system will have power requirements that are defined by the characteristics of the power dissipating components and the mission particulars. For example, an electric unmanned air vehicle (UAV) may be utilized to provide real-time video imagery of a distant "target." The aircraft's propulsion motor–propeller combination, avionics, video camera, and transmitters all have power requirements that may change with each phase of the mission: launch, climb to altitude, steady-level flight to "target", descent, loiter in surveillance, climb to altitude, steady-level flight back "home", descent, and landing. The total power required during each phase can be determined and integrated over time to determine the total energy required for a mission. Design and optimization of the subsystems (e.g., power-supply, motor–propeller, aerodynamics, etc.), which are mathematically coupled with the system performance metric, can be performed to minimize the energy/power required during the various phases of the mission. Some of the key hybrid power-system design variables include the energy delivery capacity as a function of power draw rate (i.e., Ragone curve) and the battery and scavenging hardware weights and sizes.

The following example is provided to illustrate the nature of the design calculations. Let the flight endurance time (t_E) of an electric UAV under steady-level flight conditions be the system performance metric of interest. An equation for t_E with both battery and solar scavenging power sources can be obtained by modifying Eq. (2) in Ref. [49] as follows:

$$t_E = \frac{E_B\eta_B + P_{SC}t_E}{W_T^{3/2}}\left[\frac{\rho S C_L^3}{2C_D^2}\right]^{1/2}\eta_{M-P}$$

$$\rightarrow t_E = \frac{E_B\eta_B}{\left(W_T^{3/2} - P_{SC}\left[\frac{\rho S C_L^3}{2C_D^2}\right]^{1/2}\eta_{M-P}\right)}\left[\frac{\rho S C_L^3}{2C_D^2}\right]^{1/2}\eta_{M-P} \tag{21}$$

In Eq. (21), E_B is the nominal battery energy, η_B an efficiency factor that accounts for the affect of discharge power, temperature, etc., on the deliverable energy, W_T the total vehicle weight ($m_T g$), P_{SC} the solar scavenger output power, ρ the air mass density, S the wing platform area, C_L and C_D the lift and drag coefficients, and η_{M-P} is an efficiency factor that accounts for the conversion of electrical power into thrust power by the motor and propeller.

Normalized change in endurance, $\Delta t_E/t_E$, as a function of changes in battery energy, subsystem weights, and/or scavenger power can be approximated using a Taylor series expansion of Δt_E about the point $P_{SC} = 0$ (i.e., linear extrapolation from the non-solar design):

$$\frac{\Delta t_E}{t_E} = \frac{\Delta E_B}{E_B} - \frac{3}{2}\frac{\Delta W_T}{W_T} + \frac{\Delta P_{SC}}{\frac{E_B}{t_E}} = \frac{\Delta m_B}{m_B} - \frac{3}{2}\frac{\Delta m_B + \Delta m_{ST} + \Delta m_{SC}}{m_T} + \frac{p_{SC}}{p_{ave}}\frac{\Delta m_{SC}}{m_B} \tag{22}$$

Δm_B, Δm_{ST}, Δm_{SC} denote the changes in battery, structure, and photonic scavenger masses, p_{SC} denotes the specific power of the solar scavenger system (output power per unit scavenger system mass), and $p_{ave} = E_B\eta_B/m_B t_E$ is the average specific power supplied by the battery system in the non-solar version of the UAV.

Eq. (22) can be used to assess how solar scavenging influences the flight endurance time of an electric UAV. For example, consider the following five design scenarios: (1) add a solar scavenger system to the UAV without changing the existing battery or vehicle structure weights; (2) add a solar scavenger system to the UAV and remove an equal amount of battery weight while keeping the structure weight constant; (3) add a solar scavenger system to the UAV and remove an equal amount of structure weight (multifunctional solution) while keeping the battery weight constant; (4a) add more battery to the UAV without adding a solar scavenger and without changing the structure weight, or (4b) add more battery to the UAV and remove an equal amount of structure weight (multifunctional solution), again without adding a scavenger system. Cases 4a and 4b serve as "standards" for comparing solar scavenging with battery addition as a means of increasing UAV endurance. Cases 1 and 4a consider changes in endurance through solar scavenger or battery addition, respectively, without any other design changes. Cases 3 and 4b consider changes in endurance through substitution of solar scavenger or battery weight, respectively, for UAV structure (multifunctional design). Case 2 is similar to Case

Table 5
Expressions for the normalized change in flight endurance time, $\Delta t_E/t_E$, as a function of changes in battery, structure, or solar scavenger mass: Δm_B, Δm_{ST}, Δm_{SC}; specific output power of the solar scavenger, p_{SC}, and average discharge power per unit on-board battery mass, p_{ave}

Case	Conditions	Normalized change in flight endurance, $\Delta t_E/t_E$	$(\Delta t_E/t_E)_{m\text{-UAV}}$	Rank
1	$\Delta m_B = \Delta m_{ST} = 0$	$-\frac{3}{2}\frac{\Delta m_{SC}}{m_T} + \frac{p_{SC}}{p_{ave}}\frac{\Delta m_{SC}}{m_B}$	$\{-0.0067 + 3.33\times10^{-5} p_{SC}\}\Delta m_{SC}$	2
2	$\Delta m_B = -\Delta m_{SC}$, $\Delta m_{ST} = 0$	$-\frac{\Delta m_{SC}}{m_B} + \frac{p_{SC}}{p_{ave}}\frac{\Delta m_{SC}}{m_B}$	$\{-0.0133 + 3.33\times10^{-5} p_{SC}\}\Delta m_{SC}$	3
3	$\Delta m_{ST} = -\Delta m_{SC}$, $\Delta m_B = 0$	$\frac{p_{SC}}{p_{ave}}\frac{\Delta m_{SC}}{m_B}$	$\{3.33\times10^{-5} p_{SC}\}\Delta m_{SC}$	1
4*a*	$\Delta m_{SC} = \Delta m_{ST} = 0$	$\frac{\Delta m_B}{m_B} - \frac{3}{2}\frac{\Delta m_B}{m_T}$	$\{0.0067\}\Delta m_B$	2
4*b*	$\Delta m_{ST} = -\Delta m_B$, $\Delta m_{SC} = 0$	$\frac{\Delta m_B}{m_B}$	$\{0.0133\}\Delta m_B$	1

The two right columns pertain to a notional micro-UAV with a total mass of 225, 75 g of battery with a specific energy of 200 Wh kg^{-1}, and 30 min of flight time.

3 except that solar scavenger weight is substituted for battery weight.

Table 5 summarizes the general relations derived from Eq. (22) for each of the design scenarios and their application in each case to a notional micro-UAV with the following specifications: total vehicle mass of 225, 75 g of secondary lithium-ion cells with 200 Wh kg^{-1} providing a total of 15 Wh of battery energy, 30 min of flight endurance time, and 400 cm^2 wing area. The wing area defines a limit on the maximum number of solar cells (N) that can be attached to the UAV; $N \approx S/A_{SC}$ where S is the wing planform area and A_{SC} is the area per solar cell. The two right columns in Table 5 correspond to micro-UAV calculations.

Equating the expressions for normalized change in endurance for the micro-UAV between Cases 1 and 4a and between Cases 3 and 4b, we find that the solar scavenger system must have a specific power value:

$$p_{SC} \geq 400\,\text{W kg}^{-1} \tag{23}$$

in order to increase the micro-UAV endurance beyond that which can be achieved by simply adding more battery. Examination of these expressions also shows that the largest increase in endurance occurs with the multifunctional designs (Cases 3 and 4b) that replace structure with multifunctional structure-scavenger or structure-battery "materials" gram-for-gram. The least effective design appears to be Case 2, which replaces battery with solar scavenger. Adding solar scavenging or more battery to an existing UAV without any other design changes (i.e., Cases 1 and 4a) achieves results that are intermediate to the multifunctional (3, 4b) and battery replacement (2) design configurations.

For the solar cells listed in Table 1, the specific powers range from 180 to 560 W kg^{-1} for 1000 W m^{-2} of incident solar radiation at a zero incidence angle. These specific power quantities refer to the photovoltaic cell itself and do not include the weight of necessary auxiliary hardware needed by the scavenging system (e.g., wiring, diodes, power-conditioning electronics, and cell attachment adhesive/framing).

The angle of incidence (see Fig. 4) for solar cells fixed on the upper wing skin of an UAV (i.e., oriented parallel to the ground) is numerically equal to the UAV location latitude at noon (at vernal and autumnal equinox) and 90° at sunrise and sunset. An approximate "derating" factor to account for the change in incidence angle throughout the day can be devised by averaging Eq. (2) over the daylight hours while ignoring I_d and I_r. Let us assume that the incidence angle changes linearly with time from 90° at sunrise ($t = 0$) to the flight location latitude at noon ($t = T/2$) and then back to 90° at sunset ($t = T$); we then define:

$$\text{incidence angle derate factor, } F_{IAD} \equiv \frac{1}{T}\int_0^T \cos\theta(t)\,\mathrm{d}t \tag{24}$$

For Baltimore, MD (39.18° latitude), $F_{IAD} = 0.415$ over any arbitrary period, T, which corresponds with a constant-valued incidence angle of 65.5°. At the equator (0° latitude), $F_{IAD} = 0.637$ corresponding with constant-valued incidence angle of 50.4°. The average incidence angle will decrease when the UAV flight is shorter and centered about the noon hour resulting in the need for a less significant derate factor. For example, short flights centered about the noon hour in Baltimore would give $F_{IAD} \approx 0.75$ (i.e., cos(39.18°)).

Derate factors for Baltimore, MD can also be estimated using the data in Fig. 5. Assume that the two-axis data correspond to a zero angle of incidence. Then the ratio of flat-to-two-axis monthly averaged solar energies can be used as a measure of the decline in incident solar energy with collector orientation. For June, this ratio equals 0.764 and for December it equals 0.434. These values are roughly consistent with those computed using Eq. (24). To simplify the subsequent calculations, we will take: $F_{IAD} = 0.6$.

Derating factors for hardware performance and added auxiliary weight are also needed. We will take $F_{LOSS} = 0.862$ to account for the hardware related losses (see Footnote 3). Assuming that 10% of the total scavenger system weight is taken up by the auxiliary components gives $F_{WGT} = 0.91$. Multiplying all of these factors together gives an overall incidence/loss/weight derating factor: $F_{SC} = F_{IAD} \times F_{LOSS} \times F_{WGT} = 0.471$. We will use F_{SC} to "uprate" the specific power requirement for the solar cells (Eq. (23)) being considered for the notional micro-UAV:

$$p_{SC} \geq \frac{400}{0.471} = 849\,\text{W kg}^{-1} \tag{25}$$

The analysis has shown that solar cells with a specific power greater than 849 W kg^{-1} are required to achieve an increase in flight endurance time greater than that which can be obtained

by simply adding more battery to the aircraft. For the notional micro-UAV of this example, we cannot meet the required solar cell performance with any of the cells listed in Table 1. Adding battery is more effective in increasing endurance, in this example, than adding solar scavenging.

If the UAV mission is such that it requires an in-the-field recharging capability that can only be achieved using solar scavenging, then the requirement expressed by Eq. (25) must be relaxed. We drop that requirement that the solar scavenger be more effective than battery and require only that it leads to a positive increase in endurance (i.e., $\Delta t_E \geq 0$). From the expressions in Table 5, we can see that the flight endurance time always increases when $p_{SC} \geq 0$ for Case 3 (multifunction swapping of structure for scavenger), or when $p_{SC} \geq 200/0.471 = 425\,W\,kg^{-1}$ for Case 1 (addition of scavenger). Multifunctional swapping of solar scavenger mass for structure mass will always provide an increase in endurance, regardless of the solar scavenger system efficiency. If the solar scavenger is added to the micro-UAV without any other changes, then solar cells with a specific power greater than $425\,W\,kg^{-1}$ are required to achieve an increase in flight endurance time. The SunPower® Pegasus cells from Table 1 meet this specific power requirement; the Pegasus cells are used on AeroVironment's Pathfinder and Helios solar-powered UAVs.

The above example shows how quantitative system performance metrics, flight endurance time in this case, can be used to assess design options related to the energy scavenging and storage subsystems. Additional system requirements/constraints not addressed by the primary system performance metric are often necessary and will influence the design solution space. The requirement for in-the-field solar charging capability is an example of this; it opened-up the design space so that "suboptimal" solar cells ($425\,W\,kg^{-1}$ versus $850\,W\,kg^{-1}$) became viable options. Refinements of the analysis are possible by going beyond the Taylor series expansion (linear extrapolation) for Δt_E, using actual solar radiation data for the operational locations and mission times, and by considering combinations of the three design scenarios.

4. Summary

A variety of energy scavenging concepts for supplementing the on-board energy store of small electric unmanned systems have been reviewed and analyzed. Scavenger system output power depends on the availability of scavengable energy in the environment, the size/weight of the energy collection elements, the efficiency of collection, and the efficiency of conversion to electric system energy. Power collection capability (e.g., specific power values), conversion efficiencies, weights, and sizes, plus magnitude estimates for the availability of each type of scavengable energy have been reported. Solar (photonic) energy is readily available outdoors and can be collected by both mobile and immobile systems. Solar scavenging systems can be developed using commercial technology and are capable of providing on the order of ~1 to 10 W of power depending on the area available for collection. Kinetic (wind) flow and thermal energies are also readily available in many locations, though at lower average levels than solar energy. Kinetic and thermal scavenging systems can be developed using commercially available technology to provide power in the 10^{-2} to 1 W range. Electromagnetic (EM) energy is available in select locations, and EM scavenging systems have to be custom designed and fabricated. They have a wide range of power collection capability, from $\sim 10^{-3}$ to tens of Watts. Multifunctional autophagous structure–power technology can provide supplemental energy from the consumption and conversion of system materials. They must be custom designed and fabricated and can supply ~1 to 10 W of power. A common design challenge for energy scavenging for small-scale applications is minimizing the mass and volume auxiliary hardware relative to the energy collection components.

Acknowledgements

This work was supported through Naval Research Laboratory's Core Research Program. The motor–generator and autophagous data were provided by Mr. William Pogue in NRL-Code 6350.

References

[1] L. Christodoulou, J.D. Venables, JOM 55 (2003) 39–45.
[2] J.P. Thomas, M.A. Qidwai, Acta Mater. 52 (2004) 2155–2164.
[3] J.P. Thomas, M.A. Qidwai, JOM 57 (2005) 18–24.
[4] Renewable Resource Data Center (RReDC), 2005. http://rredc.nrel.gov/.
[5] S. Roundy, P.K. Wright, J.M. Rabaey, Energy Scavenging for Wireless Sensor Networks with Special Focus on Vibrations, Kluwer Academic Press, Boston, MA, 2004.
[6] A. Chandrakasan, R. Amirtharajah, S. Cho, J. Goodman, G. Konduri, J. Kulik, W. Rabiner, A. Wang, Design considerations for distributed microsensor systems, in: Proceedings of IEEE Custom Integrated Circuits, IEEE, San Diego, CA, 1999.
[7] A. Kansal, M.B. Srivastava, An environmental energy harvesting framework for sensor networks, in: Proceedings of International Symposium on Low Power Design, Seoul, Korea, 2003.
[8] M. Rahimi, H. Shah, G.S. Sukhatme, J. Heideman, D. Estrin, Studying the feasibility of energy harvesting in a mobile sensor network, in: Proceedings of IEEE International Conference on Robotics and Automation, Taipei, Taiwan, 2003.
[9] G.W. Taylor, J.R. Burns, S.A. Kammann, W.B. Powers, T.R. Welsh, IEEE J. Ocean. Eng. 26 (2001) 539–547.
[10] N.S. Shenck, J.A. Paradiso, IEEE Micro 21 (2001) 30–42.
[11] J. Edmison, M. Jones, Z. Nakad, T. Martin, Using piezoelectric materials for wearable electronic textiles, in: Proceedings of Sixth International Symposium on Wearable Computers (ISWC), Seattle, WA, 2002.
[12] P. Glynne-Jones, S.P. Beeby, N.M. White, Towards a piezoelectric vibration-powered microgenerator, in: Proceedings of IEEE Science, Measurement and Technology, IEEE, 2001.
[13] T. Sterken, K. Baert, R. Puers, S. Borghs, Power extraction from ambient vibration, in: Proceedings of SeSens Workshop on Semiconductor Sensors, Veldhoven, The Netherlands, 2002.
[14] D. Pescovitz, The Power of Small Tech, 2004. http://www.smalltimes.com/document_display.cfm?document_id=3730.
[15] R. Chevalier, Juice on the Loose, 2002. http://www.newscientist.com.
[16] P.B. Koeneman, I.J. Busch-Vishniac, K.L. Wood, J. Microelectromechan. Syst. 6 (1997) 355–362.
[17] K. Najafi, Low-power micromachined microsystems, in: Proceedings of International Symposium on Low Power Electronics and Design, 2000.
[18] S.A. Jacobson, A.H. Epstein, An informal survey of power Mems, in: Proceedings of International Symposium on Micro-Mechanical Engineering, Paper # Ismme2003-K18, Tsukuba, Japan, 2003.

[19] J.W. Stevens, Heat transfer and thermoelectric design considerations for a ground-source thermo generator, in: Proceedings of 18th International Conference on Thermoelectrics, 1999.
[20] E.E. Lawrence, G.J. Snyder, A study of heat sink performance in air and soil for use in a thermoelectric energy harvesting device, in: Proceedings of 21st International Conference on Thermoelectrics (ICT '02), 2002.
[21] S. Jung, C. Lauterbach, M. Strasser, W. Weber, Enabling technologies for disappearing electronics in smart textiles, in: Proceedings of International Solid-State Circuits Conference, IEEE, 2003.
[22] J. Fleming, W. Ng, S. Ghamaty, J. Aircraft 41 (2004) 674–676.
[23] M.R. Patel, Wind and Solar Power Systems, CRC Press LLC, Boca Raton, FL, 1999.
[24] J.L. Stone, Phys. Today 46 (1993) 22–29.
[25] J.C. Wiles, D.L. King, Blocking diodes and fuses in low-voltage Pv systems, in: Proceedings of 26th Photovoltaic Specialists Conference, IEEE, 1997.
[26] M.A. Green, K. Emery, D.L. King, S. Igari, W. Warta, Prog. Photovolt. Res. Appl. 13 (2005) 387–392.
[27] T. Teich, Advances in thin-film copper indium gallium diselenide (Cigs) solar power, in: Proceedings of 41st Power Sources Conference, Philadelphia, PA, 2004.
[28] W. Marion, S. Wilcox, Solar Radiation Data Manual for Flat-Plate and Concentrating Collectors, NREL/TP-463-5607, National Renewable Energy Laboratory, 1994.
[29] E. Coffari, The Sun and the Celestial Vault, in Solar Energy Engineering, Academy Press, Inc., New York, 1977, pp. 5–27.
[30] A.B. Meirel, M.P. Meirel, Applied Solar Energy—An Introduction, Addison-Wesley Publishing Co., Reading, MA, 1976.
[31] PVWATTS, A Performance Calculator for Grid-Connected Pv Systems, 2005. http://rredc.nrel.gov/solar/calculators/PVWATTS/version1/.
[32] R.E. Wilson, P.B.S. Lissaman, Applied Aerodynamics of Wind Power Machines, NSF RANN GI-41840, Oregon State University, 1974, pp. 1–106.
[33] F. Eldridge, Wind Machines, 2nd ed., Van Nostrand Reinhold, New York, 1980.
[34] D.K. Benson, T.S. Jayadev, Thermoelectric energy conversion—economical electric power from low grade heat, in: Proceedings of Energy Technology Conference, 1980.
[35] K. Matsuura, D.M. Rowe, Low temperature heat conversion, in: CRC Handbook of Thermoelectrics, CRC Press LLC, Boca Raton, FL, 1995, pp. 573–593.
[36] A.W. Culp, Principles of Energy Conversion, McGraw-Hill, New York, 1979.
[37] D.M. Rowe, CRC Handbook of Thermoelectrics, CRC Press LLC, Boca Raton, FL, 1995.
[38] H.J. Goldsmid, Conversion efficiency and figure-of-merit, in: CRC Handbook of Thermoelectrics, CRC Press LLC, Boca Raton, FL, 1995, pp. 19–25.
[39] D.M. Rowe, G. Min, J. Power Sources 73 (1998) 193–198.
[40] B. Berland, Photovoltaic Technologies Beyond the Horizon: Optical Rectenna Solar Cell, NREL/SR-520-33263, National Renewable Energy Laboratory (NREL), 2003, http://www.nrel.gov/docs/fy03osti/33263.pdf.
[41] B. Berland, L. Simpson, G. Nuebel, T. Collins, B. Lanning, Optical Rectenna for Direct Conversion of Sunlight to Electricity, National Renewable Energy Laboratory (NREL), 2001, http://www.nrel.gov/ncpv_prm/pdfs/papers/54.pdf.
[42] R. Corkish, M.A. Green, T. Puzzer, T. Humphrey, Solar Energy 73 (2002) 395–401.
[43] J. Troitzsch, International Plastics Flammability Handbook, 2nd ed., Hanser Publishers, Munich, 1990.
[44] L.J. Giacoletto, Energy Storage Convers. 2 (2) (1965) 95.
[45] J.N. Baucom, J.P. Thomas, W.R. Pogue III, M.A. Qidwai, Autophagous structure–power systems, in: Proceedings of SPIE, The International Society for Optical Engineering, San Diego, CA, 2004.
[46] W.R. Pogue III, J.N. Baucom, J.P. Thomas, M.A. Qidwai, Structure–power system for unmanned vehicles, in: Proceedings of AUVSI Unmanned Systems North America, Autonomous Unmanned Vehicle Systems International, Baltimore, MD, 2005.
[47] M.C.Y. Nui, Composite Airframe Structures, Hong Kong Conmilit Press Ltd., 1992, pp. 122–123.
[48] T. Christen, M.W. Carlen, J. Power Sources 91 (2000) 210–216.
[49] J.P. Thomas, M.A. Qidwai, P. Matic, R.K. Everett, A.S. Gozdz, M.T. Keennon, J.M. Grasmeyer, Structure–power multifunctional materials for Uav's, in: Proceedings of SPIE Conference on Smart Materials and Structures, Paper# 4698-17, SPIE, San Diego, CA, 2002.